RESEARCH ARTICLE

Journal
American Ceramic Society

Near-surface plastic deformation in polycrystalline SrTiO₃ via room-temperature cyclic Brinell indentation

Chukwudalu Okafor[1,2] | **Kuan Ding**[1,3] | **Oliver Preuß**[1] | **Neamul Khansur**[4] | **Wolfgang Rheinheimer**[5] | **Xufei Fang**[1,2]

[1]Department of Materials and Earth Sciences, Technical University of Darmstadt, Darmstadt, Germany

[2]Institute for Applied Materials, Karlsruhe Institute of Technology, Karlsruhe, Germany

[3]Max Planck Institute for Sustainable Materials, Düsseldorf, Germany

[4]Department of Materials Science and Engineering, Friedrich-Alexander-Universität Erlangen-Nürnberg (FAU), Erlangen, Germany

[5]Institute of Manufacturing Technologies of Ceramic Components and Composites, University of Stuttgart, Stuttgart, Germany

Correspondence
Chukwudalu Okafor, Department of Materials and Earth Sciences, Technical University of Darmstadt, Darmstadt, Germany.
Email: chukwudalu.okafor2@kit.edu

Editor's Choice
The Editor-in-Chief recommends this outstanding article.

Abstract

Dislocations are being used to tune versatile mechanical and functional properties in oxides with most current studies focusing on single crystals. For potentially wider applications, polycrystalline ceramics are of concern, provided that dislocations can be successfully introduced. However, in addition to preexisting pores and flaws, a major barrier for bulk plastic deformation of polycrystalline ceramics lies in the grain boundaries (GBs), which can lead to dislocation pile-up and cracking at the GBs due to the lack of sufficient independent slip systems in ceramics at room temperature. Here, we use the cyclic Brinell indentation method to circumvent the bulk deformation and focus on near-surface regions to investigate the plastic deformation of polycrystalline SrTiO₃ at room temperature. Dislocation etch-pit analysis suggests that plastic deformation can be initiated within the grains, at the GBs, and from the GB triple junction pores. The deformability of the individual grains is found to be dependent on the number of cycles, as also independently evidenced on single-crystal SrTiO₃ with representative surface orientations (001), (011), and (111). We also identify a grain-size-dependent plastic deformation.

KEYWORDS
cyclic indentation, dislocation, plasticity, strontium titanate, surface deformation

1 | INTRODUCTION

Recent advances in dislocation-mediated functional properties of ceramic oxides have re-ignited the research interest in plastically deformable ceramics for dislocation engineering, which is a prerequisite for harvesting dislocation-tuned properties.[1–3] Aside from the mainstream high-temperature deformation for dislocation

imprint into ceramics,[4,5] research on room-temperature dislocation engineering (with earlier works on MgO,[6] CaF$_2$,[7] KNbO$_3$,[8] and LiF,[9]) has made promising progress. Recently, high-density dislocations (up to $\sim 10^{14}$/m^2) with plastic zone size up to millimeter/centimeter (in length) at room temperature without cracking have been achieved in single-crystal ceramics such as SrTiO$_3$ (STO),[10,11] KNbO$_3$,[12] CaF$_2$,[11] and ZnS.[13] In contrast to single crystals, polycrystalline ceramics remain desirable candidates for potential large-scale and wider application due to their much lower cost and relatively easier fabrication.

Room-temperature plastic deformation on polycrystalline ceramics has been a subject of complexity, and in general, often considered not feasible. From a mechanics point of view, there is an insufficient number of independent slip systems in ceramics at room temperature—as five independent slip systems are required for general plastic deformation of bulk polycrystals according to the von Mises or Taylor criterion,[14–16] whereas most ionic and covalent bonded ceramics have only two independent slip systems at room temperature.[14,17] The limited independent slip systems could result in dislocation pile-up at the grain boundaries (GBs),[18,19] namely, preventing slip transmission through GBs[20] and leading to crack formation.[21,22] Second, the fabrication route for most ceramics involves sintering at elevated temperatures,[23] often leaving the ceramics with extremely low dislocation densities at such temperatures (e.g., $\sim 10^9$/m^2 for conventionally sintered STO[24,25]) and making dislocation nucleation necessary prior to dislocation-mediated plastic deformation takes place. However, the nucleation of dislocations requires extremely high stresses close to the theoretical shear strength (e.g., $\sim$17 GPa for STO[26,27]), and often fracture precedes instead. Additionally, pores and flaws formed during the synthesis and/or microcracks induced during the machining of ceramics are most widely accepted as sources of stress concentration and location for crack initiation and propagation.

Various studies on the plastic deformation (accompanied by cracking) of polycrystalline rock-salt ceramics via mechanical deformation at ambient temperature are available in the literature.[28–30] For example, MgO has a cubic structure and was heavily studied in history. Sinha et al.[28] observed that dislocations were initiated from sources in the vicinity of GBs in polycrystalline MgO (average grain size $\approx$ 10 μm) during tensile testing. Nevertheless, microcracking occurs at the intersection of two groups of slip bands, leading to fracture.[28] Earlier observations by Westwood[31] on bi-crystal MgO deformed in compression showed the piling-up of groups of edge dislocations at the grain boundary. A single group of edge dislocations will not necessarily nucleate cracks at the grain boundary, but rather two groups.[31] Moriyoshi et al.[32] confirmed that dur-

ing in situ tensile deformation of bicrystal MgO, fracture does not necessarily occur at the grain boundary but about 50–200 nm away from the grain boundary while cracks form by the Zener–Stroh mechanism.[32]

To overcome the insufficient number of slip systems in ceramics at room temperature, deformation at high temperatures is necessarily adopted, with additional high-temperature slip systems being activated to satisfy the von Mises or Taylor criterion. For example, in perovskite oxides, the $< 1\bar{1}0 > \{110\}$ group of slip systems (room temperature, also active at elevated temperatures) and $< 1\bar{1}0 > \{001\}$ (elevated temperature)[33] providing additional independent slip systems; hence, STO has the required five independent slip systems only at elevated temperatures. Additionally, through thermal activation, new dislocation sources[34,35] can be activated, and the dislocation mobility can also be increased with temperature within the ductile regime of STO.[33] Porz et al.[24] reported that polycrystalline STO could withstand more than 4% plastic strain without fracture during a bulk uniaxial compression test performed above 1050°C. They also observed a three orders of magnitude increase in the dislocation density (between the pristine $\sim 6 \times 10^9$/m^2 and deformed sample $\sim 3 \times 10^{12}$/m^2) using an ultrahigh voltage electron microscope in the scanning transmission electron microscope mode.[24] Similarly, high-temperature dislocation studies on polycrystalline MgO over a broad temperature range (800–1400°C) revealed that at temperatures between 800 and 1200°C, dislocation glide governs the plastic deformation.[36] However, grain boundary sliding dominates above 1200°C,[37] leading to potential competition between grain boundary sliding, thermally aided diffusion, thermally activated dislocation creep/climb, and dislocation-mediated plasticity at elevated temperatures.[38]

Here, we focus on the following pertinent questions: knowing the limitations of bulk plasticity of ceramics at room temperature as discussed above, can we circumvent them to introduce a high dislocation density in polycrystalline ceramics without fracture? It was suggested by Groves et al.[17] that fracture does not necessarily occur if five independent slip systems are not available. Hence, we start with the working hypothesis that the free surfaces of polycrystalline samples can, in principle, relax the von Mises or Taylor criterion by avoiding dislocation pileup. Would it then be possible to plastically deform polycrystalline ceramics in the near-surface regions? In addition, it is well known that grain size can play an important role in the mechanical properties of polycrystalline ceramics. How would the grain size influence the room-temperature plasticity (if at all)?

To answer the above questions, we use a Brinell indenter equipped with a hardened-steel sphere to induce plastic deformation on polycrystalline STO (with varying

TABLE 1 Polycrystalline STO samples with their corresponding grain sizes.

Sample	Average grain size (µm)	Relative density (%)
Type X	50	96
Type Y1	20	98
Type Y2	1	98
Type Z	0.2	N/A

grain sizes) by cyclic Brinell indentation. In what follows, we first adopt the experimental approach introduced previously on single-crystal STO with (001) surface orientation[10] and extend it to single-crystal STO with (011) and (111) surface orientations. With the insights gained from analyzing the dislocation structure and slip traces on single crystals with these three basic crystal orientations, we further investigate the deformation of polycrystalline STO surfaces with more random crystallographic orientations. Finally, we discuss the influence of GBs and triple junction pores on the plasticity of polycrystalline STO based on the experimental observation.

2 | METHODS

2.1 | Materials and experimental procedures

For benchmarking purposes, undoped single-crystal STO samples with representative surface orientations (001), (011), and (111) were tested first, which provided a better understanding of the dislocation slip trace patterns after the Brinell indentation (details on mechanical testing given in Section 2.2). The samples have a geometry of $10 \times 10 \times 1$ mm^3 with one side polished (Alineason Materials Technology GmbH, Frankfurt am Main, Germany).

To achieve different average grain sizes, three different approaches were used to synthesize the polycrystalline samples. As summarized in Table 1, Type X was conventionally sintered with an average grain size of ~50 µm and density of 4.93 g/cm^3 measured using the Archimedes method (relative density of 96.4% and the theoretical density of STO is 5.11 g/cm^3).[39] The sample was pre-sintered in oxygen at 1425°C for 1 h and annealed at 1480°C in 95% N$_2$–5% H$_2$ for 6 h.[40] A final chemical etching step was carried out to reveal the dislocation etch-pits, with the samples being immersed in KOH solution (neutralized in 1 M of H$_2$SO$_4$ for 1 min) at 500°C for 15 min. Type Y was prepared by flash sintering having a grain size gradient from ~20 µm (Type Y1) to ~1 µm (Type Y2) in different sample regions due to the positioning of the electrodes.[41] Details of the synthesis of the Type Y polycrystalline STO sample can be found elsewhere.[41,42] In Type Z sample, STO powders

were deposited onto 5 mm × 5 mm × 1 mm single-crystal STO substrate via aerosol deposition,[43] where a slit nozzle with a rectangular orifice with 0.5 mm was used to accelerate N$_2$ carrier gas at a rate of 4 L/min, keeping a distance of 7 mm between the nozzle and substrate. The final film thickness of the nanocrystalline STO was 16 µm.

To achieve a smooth surface for mechanical deformation, the polycrystalline samples were hand-ground with P800, P1200, P2500, and P4000 wet grinding sandpaper (QATM). Semi-automated polishing steps (Phoenix 4000, Buehler) were subsequently performed using diamond polishing pastes with particle sizes of 6, 3, 1, and 0.25 µm for 10 min each. A final vibrational polishing step was done using an OP-S solution (~250 nm colloidal silica particles, from Struers GmbH) for 16 h.

To reveal the cross section of the sample (in this case, the (001) single crystal) for in-depth information, the deformed sample was subjected to a sequential grinding and polishing step (adopting the same polishing and grinding steps as stated above). The final polishing step using the OP-S solution ensures a smooth surface finish, ruling out possible polishing-induced dislocation during the sequential grinding and polishing. Brinell indents were performed 200 µm away from the sample edge, close enough to reach the plastic zone via grinding, but far enough to avoid cracking due to stress concentration at the edge. A detailed illustration is given in Figure S1. The chemical etching method was used to reveal the dislocation etch-pits on the single-crystal sample, which was immersed in a solution containing 15 mL 50% HNO$_3$ with 16 drops of 50% HF for 20 s.

2.2 | Room-temperature deformation and characterization

A universal hardness testing machine (Finotest, Karl-Frank GmbH, Weinheim-Birkenau, Germany) equipped with a hardened-steel sphere was used to perform the room-temperature indentation test. The ball diameter is 2.5 mm and, a constant load of 1.5 kgf was applied for the cyclic indentation. We used the number of cycles of 1× (single cycle) and 10× (10 cycles). The technical procedure for this experimental approach has been explained in detail in our previous work.[10] For each testing condition, at least 10 indents were made on each sample for statistical analysis. The surface slip traces after deformation were captured using an optical microscope (ZEISS Axio Imager 2, Carl Zeiss Microscopy GmbH) with the circular-differential interference contrast mode for a better enhancement of the surface deformation features. The slip traces and other microstructures such as etch-pits, pores, and GBs were visualized using a laser confocal microscope (LEXT OLS4000, Olympus IMS, Waltham, USA).

2.3 | EBSD mapping for polycrystalline STO

To identify the crystallographic orientations of Type X polycrystalline STO, electron-backscattered diffraction (EBSD, EDAX DigiView EBSD, EDAX) was carried out in the SEM (TESCAN MIRA3-XM SEM, Brno, Czech Republic). Characterizing this sample using EBSD proved to be easier compared to the other polycrystalline samples because of the relatively larger average grain size and visible slip trace. An area of 0.35×2 mm^2 with a step size of 1 μm was mapped on the Type X STO sample after Brinell indentation, knowing that the influence of lattice rotation on surface grains is dependent on the degree of applied stress.[44] Six representative indents (three indents for 1× and three indents for 10× tests) were placed within the mapped area. The crystallographic orientations of the grains were analyzed by the OIM analysis software (EDAX, Pleasanton, USA). The inverse pole figure was obtained from the EBSD data, with z being the out-of-plane direction.

The Schmid law describes the relationship between the applied stress and the critical resolved shear stress on a favorable slip plane and direction for uniaxially deformed samples.[45] Due to the complex stress state underneath the spherical indenter, we refer to the Schmid factor in this work as the pseudo-Schmid factor (m_{sp}), noting the difference to the Schmid factor calculated for uniaxial loading. Having the information of room-temperature active slip systems and the out-of-plane orientation of individual grains from EBSD, we calculated the Schmid factor of each deformed grain by resolving the shear stress with respect to the surface orientation for the grains within the deformed region.

3 | RESULTS AND ANALYSES

3.1 | Slip trace pattern on single-crystal (001), (011), and (111) orientations

For simplicity and a better understanding of the surface *slip trace* patterns on different grain orientations, we first performed plastic deformation via cyclic Brinell indentation on the three representative surface orientations of single-crystal STO, namely, (001), (011), and (111). The surface *slip traces* are commonly known to result from the movement of dislocation on the free surface as featured on the three representative surface orientations in Figure 1. They correspond to the intersection of the $< 1\bar{1}0 > \{110\}$ slip systems with the indented surface. The distribution of the slip traces is rather discrete after 1× loading. By cyclic Brinell indentation, the number of slip traces increases

within the plastic zone irrespective of surface orientation. We have previously reported a similar trend on the (001) surface of STO,[10] where the increase in slip traces and dislocation densities was attributed to the dislocation multiplication mechanism, most likely via Frank-Read sources and cross slip.[10]

Figures 2A and 3A feature the optical images after 10× indentation on the (011) and (111) surfaces with the dotted lines representing the intersection of the active slip planes with the indented surface. The slip planes are perpendicular to the surface in Figure 2B and inclined at 60° with the surface in Figure 2C,D. The slip planes projected in Figure 3B–D are inclined at an angle of 35.3° with the surface. Six representative slip traces are revealed on the surface, which are evidence of dislocation activation.

Optical images of the etched top surface and crosssection of (001) surface STO sample are presented in Figure 4. Similarly, the dislocation etch-pits are quite discrete after 1× and are confined to the slip planes in the cross section. The red and blue arrows indicate the slip planes (containing the dislocation etch-pits) beneath the surface that correspond to the 3D representation in Figure 4E,F. Dashed blue lines and arrows on the top surface and cross section correspond to the diagonal (011) and (01$\bar{1}$) planes, whereas the dashed red line and arrow correspond to the horizontal (101) and (10$\bar{1}$) planes. Beneath the surface, the dislocations traveled a distance of up to ~200 μm into the bulk, whereas the density decreased with penetration depth.

3.2 | Plasticity of polycrystalline samples

The examination of samples with different grain sizes after Brinell indentation revealed several distinctive features. The optical image of Type X (Figure 5A) presents direct evidence of plastic deformation depicted by the slip traces after 1× indentation. A similar observation for Type Y1 with slip traces was also observed on the surface after 1× Brinell indentation. With decreasing average grain size ($\approx$1 μm), it became more difficult to observe changes in the surface topography induced by the optimized indentation parameters (load = 1.5 kgf, tip diameter = 2.5 mm) for small-grained samples (Types Y2 and Z). Hence, we performed a stepwise increase of the load during indentation on the samples of Types Y2 and Z. Figure 5C illustrates the indentation impression after 3 and 5 kgf loading on a Type Y2 sample. An even higher load was needed in order to create a visible impression (highlighted with arrows in Figure 5C,D) on the Type Z sample. Figure 5D presents the indentation impression of 5, 7, and 9 kgf loads on the Type Z sample. Below 5 kgf load, there was no observable impression depicting plastic deformation.
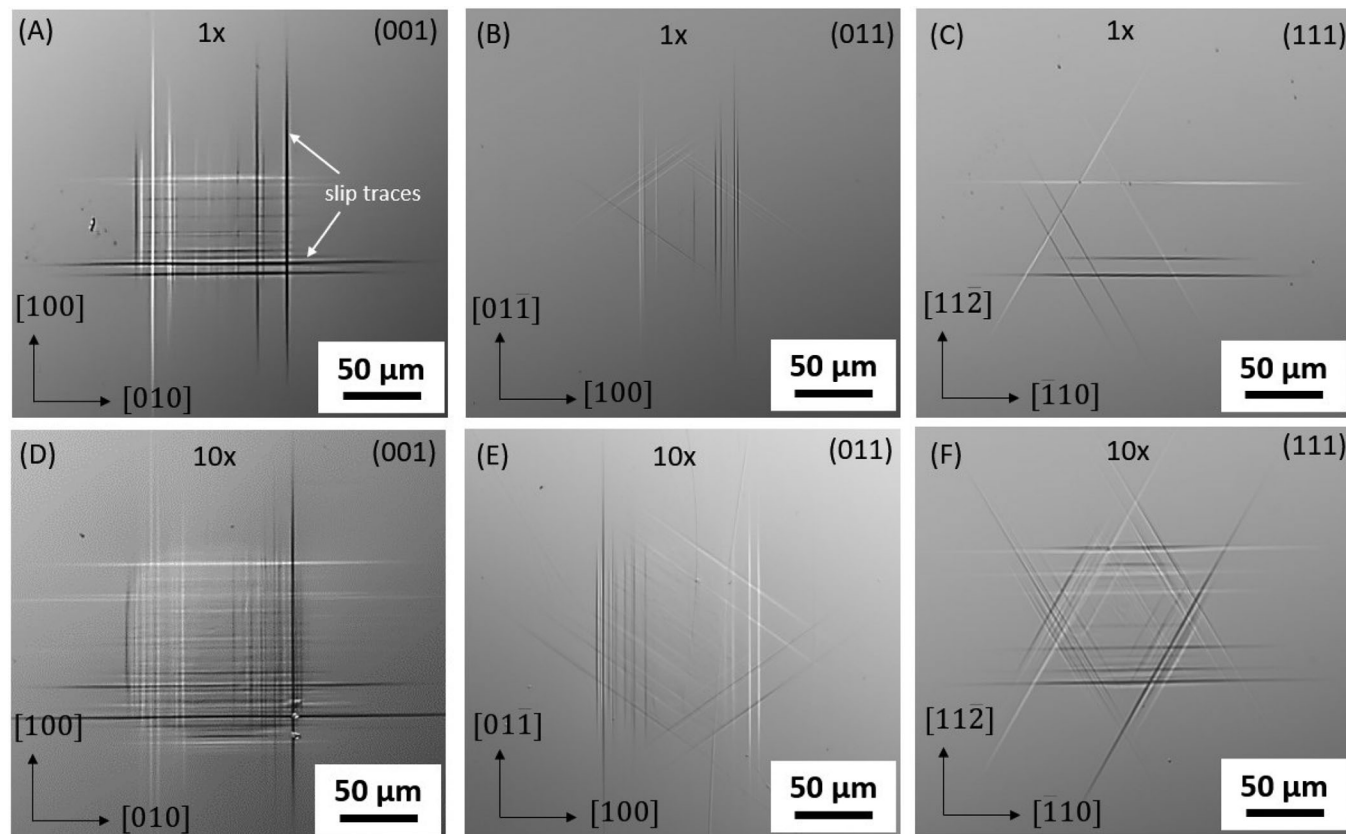
FIGURE 1 Optical microscope images depicting the slip traces (some of the slip traces are highlighted with two arrows in (A)) after 1× Brinell indentation on the (A) (001), (B) (011), and (C) (111) surface orientations of STO and after 10× cyclic Brinell indentations on (D) (001), (E) (011), and (F) (111). The slip traces are rather discrete after 1× indentation on all surface orientations (A–C), with an overall increase in the density of the slip traces after 10× indentations in (D–F) irrespective of surface orientation.
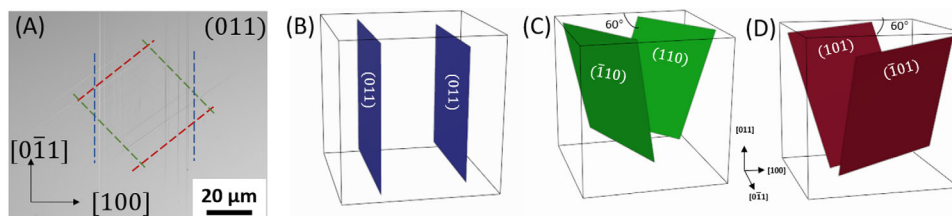

FIGURE 2 (A) Optical image after 10× indentation on the (011) surface of single-crystal STO: The slip traces are highlighted with dashed line on the surface corresponding to the intersection of the 3D projection of the activated slip planes in (B) (011) blue, (C) (110), and ($\bar{1}$10) green, and (D) (101), ($\bar{1}$01) red. There is a 60° angle of inclination between the slip planes and the indented surface in (C) and (D).
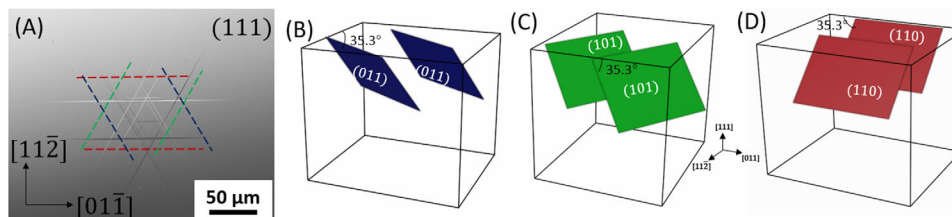

FIGURE 3 (A) Optical image after 10× indentation on the (111) surface of single-crystal STO: The slip traces are highlighted with dashed line on the surface corresponding to the intersection of the 3D projection of the activated slip planes in (B) (011) blue, (C) (101) green, and (D) (110) red. The slip planes are inclined at 35.3° to the surface.
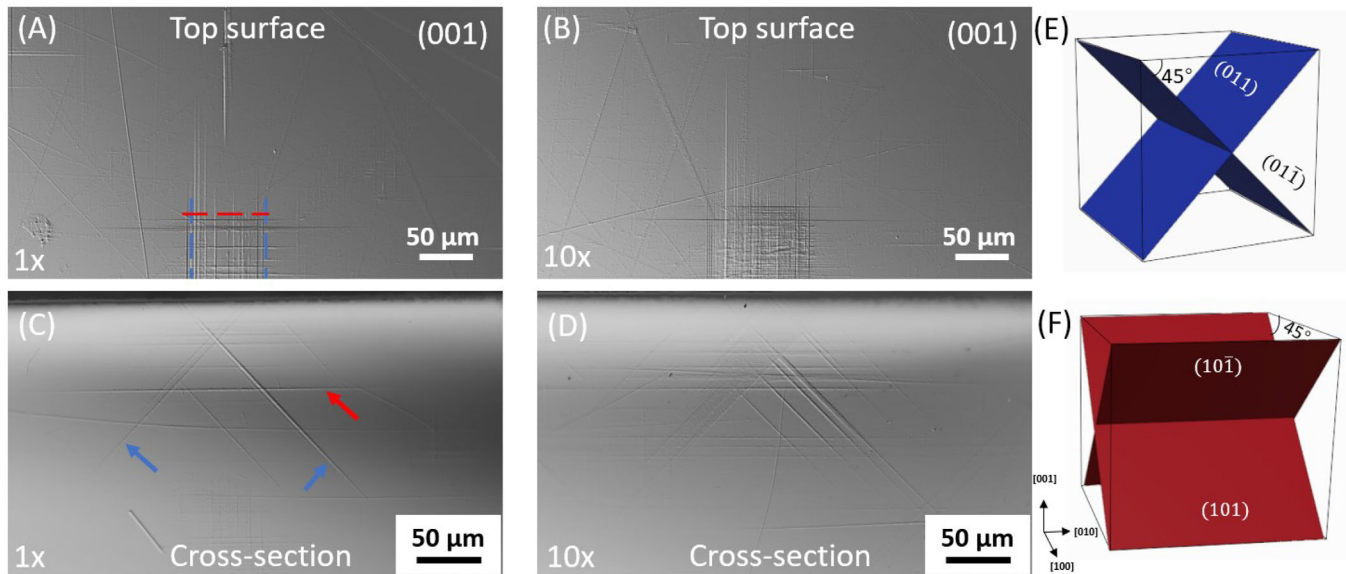
FIGURE 4 Optical image of chemically etched (001) oriented STO (A) and (B) top surface after 1× and 10× indentations, respectively, (C) cross section of indentation impression in (A), and (D) cross section of indentation impression in (B). (E) and (F) 3D representation of the active slip planes on the top surface (A) and (B), and cross section (C) and (D). Red and blue dashed lines indicate the surface slip traces in 2D, and the arrows show the etched dislocation slip traces revealed by chemical etching with the color codes corresponding to the 3D representation of the active slip planes.
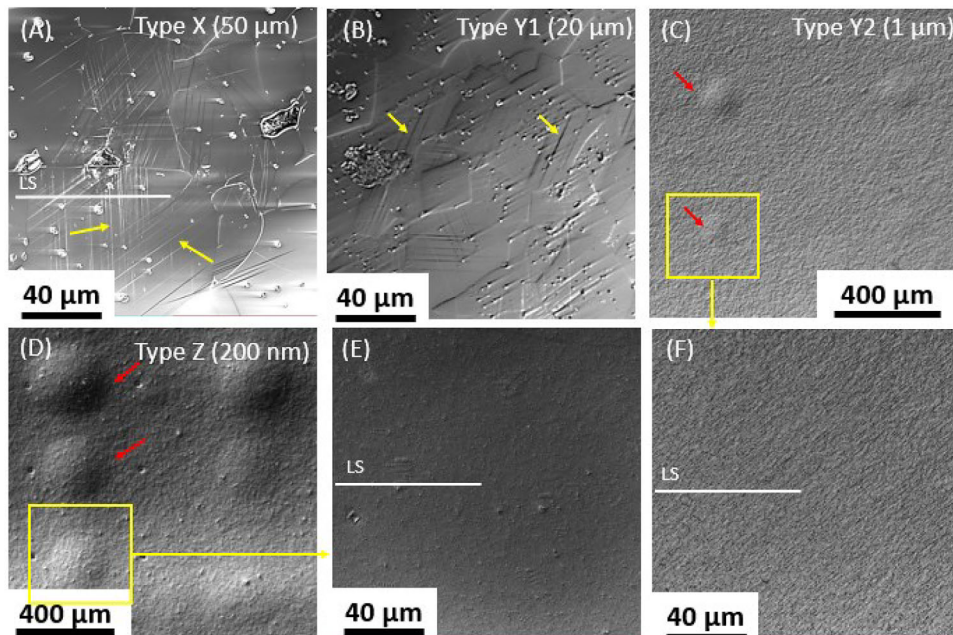

FIGURE 5 Laser scanning microscope image of polycrystalline STO samples with different average grain sizes after 10× Brinell indentation cycles. (A) Type X, average grain size = 50 µm; (B) Type Y1, average grain size = 20 µm; (C) Type Y2, average grain size = 1 µm; (D) Type Z, average grain size = 200 nm; (E) zoom into (D) showing the region deformed using 3 kgf; (F) zoom into (C) depicting the region deformed using 3 kgf. Yellow arrows in Figure 5A,B indicate the slip traces, whereas red arrows in Figure 5C,D indicate the cyclic Brinell indentation impression after 10 cycles of indentation (3 and 5 kgf in Figure 5C, respectively, and 5 and 7 kgf, respectively, in Figure 5D). LS represents the line scan of the surface topography after deformation (see Figure S2 for the line profile).
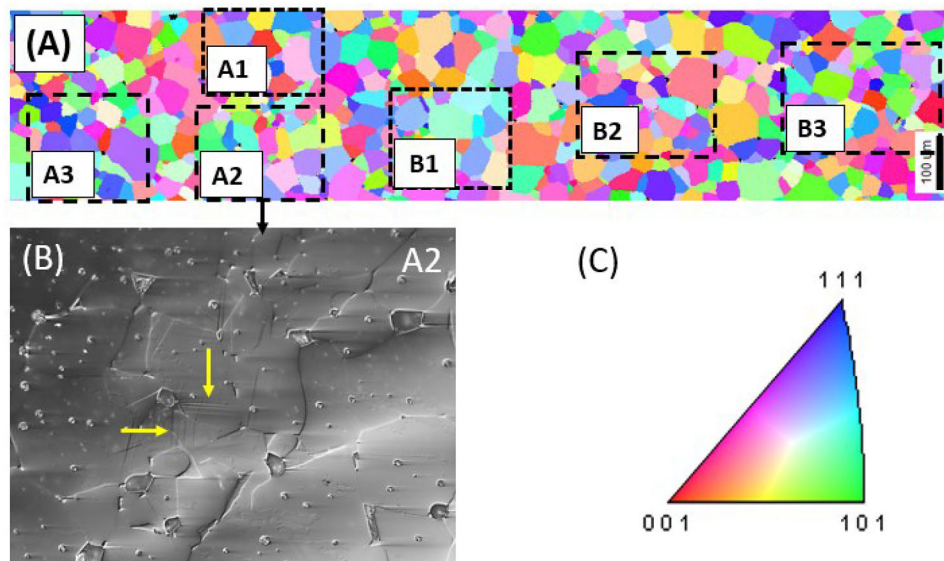
FIGURE 6 (A) Orientation mapping of Type X sample with the crystallographic orientation. (B) Optical image of position A2 after 1× indentation. (C) Inverse pole figure (IPF) legend with normal direction (ND) being the viewing direction. Yellow arrows in (B) indicate slip traces on the A2 region.

In Figure 5A,B, the slip traces are seen to disperse from a large surface triple junction pore and extend toward the adjacent GBs. Intragranular pores in Figure 5A seem to not influence the slip trace activities with the slip traces cutting through them without change in the direction. A line scan of the indentation impression of the polycrystalline samples shows a grain size–dependent plastic deformation. A much larger material displacement and larger plastic zone size were observed on a Type X sample with an average grain size of 50 μm as compared to Types Y2 and Z with average grain sizes of 1 and 0.2 μm, respectively, which suggests possible GB strengthening. This agrees with the Hall–Petch relation, which demonstrates the dependence of yield strength on the grain size of crystalline materials.[46,47] The limited plastic deformation in Types Y2 and Z is further evidenced by the smaller indentation depth presented in Figure S2, as the maximum depths of indents in Types Y2 and Z are approximately three- and sixfold smaller when compared to Type X with an average grain size of 50 μm.

3.3 | EBSD and pseudo-Schmid factor of sample Type X

To examine the individual grains and their surface orientations, an EBSD scan was performed only on the Type X sample after the indentation test because it was easier to observe the evolution of the slip traces on this sample due to the relatively larger average grain size. Figure 6 illustrates the map of the grain orientations of sample Type X.

The viewing direction is the normal direction (z-direction). The orientation distribution is visualized by color coding as illustrated in Figure 6C: that is, red for ⟨001⟩, green for ⟨101⟩, and blue for ⟨111⟩.

Within the mapped area, there are six representative deformed regions denoted by black dashed squares. Positions A1, A2, and A3 are the regions deformed by single-cycle indentation (1×), whereas B1, B2, and B3 are regions with cyclic indents up to 10 cycles (10×). Positions A1 and B1 are presented in Figure 7. The optical microscope image in Figure 7A demonstrates the slip traces after single-cycle indentation on grains A1 (highlighted using the yellow arrows). The numbering of the grains was done arbitrarily for easy identification. The contact made by the ball indenter is depicted with a dashed white circle. Only grains 1, 2, 3, and 6 present evidence of plastic deformation as seen from the surface slip traces. The pseudo-Schmid factor (m_{sp}) for these grains is larger than 0.45 except for grain 6 (with a single slip trace) as presented in Table S1. Other grain positions display no visible slip traces on the surface with a pseudo-Schmid factor lower than 0.4. A similar trend was observed for A2 and A3 deformed regions, as illustrated in Figure S3.

With cyclic Brinell indentation up to 10 cycles on positions B1, B2, and B3 (see Figure S3 for positions B2 and B3), we observed an overall increase in the slip trace densities within the contact circle (Figure 7C) similar to our previous studies on indentation[10,12,48] and scratching[2] of single-crystal STO. Interestingly, irrespective of the grain position (within the contact circle) and orientation (pseudo-Schmid factor), all grains within the contact circle
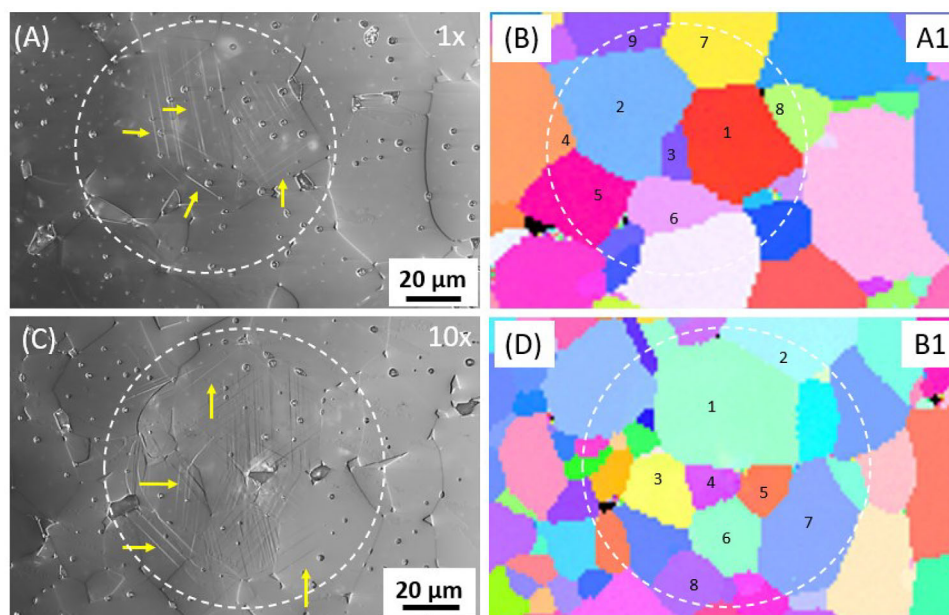
FIGURE 7 Optical microscope image highlighting slip traces after (A) 1× indentation and (C) 10× indentation corresponding electron-backscattered diffraction (EBSD) mapping in (B) and (D), respectively. The arbitrary numbering of the grains is for easy identification. Yellow arrows in (A and C) serve as a guide to identifying the slip traces on different grain positions.

in B1 display evidence of plastic deformation by slip. Most of the slip traces seem to be emitted from a single pore sitting between grains 4 and 5, and the optical microscopy observations reveal no visible macroscopic cracks. The pseudo-Schmid factor, {hkl} orientation, and Euler angles for indent positions A1 and B1 are provided in Tables S1 and S2, respectively.

3.4 | Characterization of dislocation etch-pits of Type X

The first observation from Figure 8 is the difference in the surface texture of the sample before (Figure 8A,D) and after (Figure 8B,E) chemical etching. The chemical etchant preferentially attacks the defects (dislocations, pores, and GBs) possibly due to the local high strain energy and disturbed bonding around the defects. For dislocations, chemical etching leaves behind pyramidal-shaped pits, and the geometry is dependent on the type of dislocation (edge/screw) and/or the surface orientation.[49] Optical microscopy images in Figure 8A,D reveal the slip traces after 1× indentation and 10× indentation on the Type X sample. There is an overall increase in the density of the slip traces within the contact circle and within individual grains after 10× indentation. However, not all grains with slip traces reveal etch-pits due to the difference in the surface orientation of individual grains. Grain positions 1, 2, 3, and 6 in Figure 8B do not exhibit obvious etch-pits compared to the slip traces in Figure 8A, contrasting the

observation in grain 4 where slip traces were revealed and correspond to dislocation etch-pits.

Another striking feature is the influence of the GBs and triple junction pores on the dislocation plasticity. In most cases, the dislocations (etch-pits in Figure 8C,D) are likely emitted from the GBs, extending across the grains. The dislocations in some cases (between grains 1 and 3 Figure 8E) were arrested at the grain boundary and in other cases within the grains (grain 2—Figure 8E). The current observation is in line with the work of Sinha et al.[28] on polycrystalline MgO, where grain boundary ledges serve as sources for heterogeneous nucleation of dislocations. A closer look at the boundary between grains 1 and 2 in Figure 8E indicates a possible transmission of the dislocations from grain 1 to grain 2, and it seems that transmission for dislocation–grain-boundary interaction was achieved between grains 1 and 2 (Figure 8F) but not between grains 1 and 3. Detailed studies on dislocation–grain-boundary interaction are being conducted and will be reported in the future.

Besides the GBs, the triple junction pores can also facilitate dislocation emission (Figure 8F). For instance, the pore between grains 1 and 2 in Figure 8F can be seen as the source of the dislocations that extend and terminate within grain 2. A closer examination of Figure 8C (grain 5) confirms the emission of dislocations from a triple junction pore. This can also be observed in Figure 8A,D with a high density of slip traces in the vicinity of the pores at the triple junctions. Intragranular pores appear not to influence the slip trace activities (plastic deformation). This can be seen
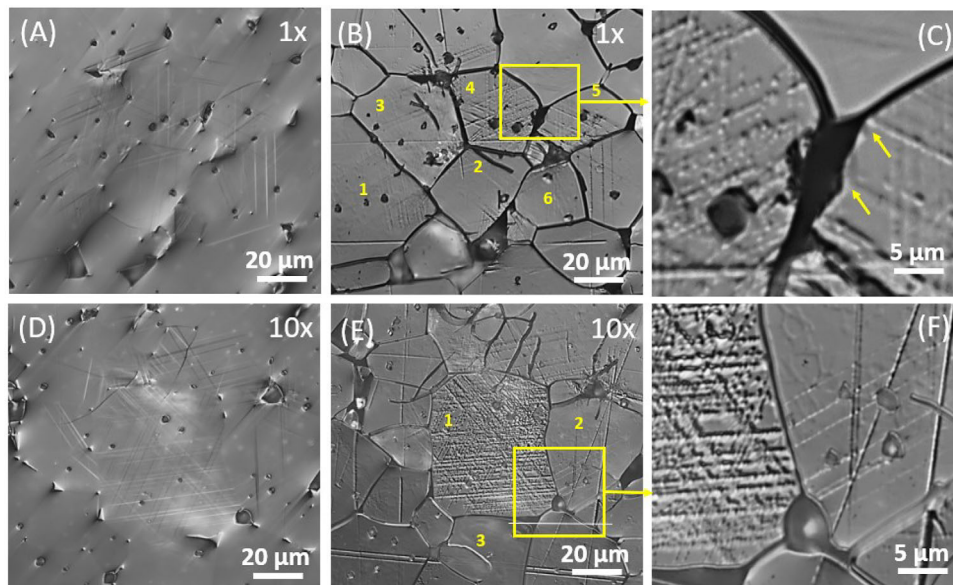
FIGURE 8 (A) Optical microscope image after a single-cycle indentation (1×), (B) after chemical etching of (A), (C) zoom into (B) with the grain boundary (GB) sources of dislocations in display. (D) Optical microscope image after 10× indentation, (E) after chemical etching of (D), and (F) a zoom into (E) revealing triple junction pore acting as initiation sites for slip. Yellow arrows serve as a guide to the etch-pit dislocations at the GB between grains 4 and 5.

by considering the direction of the slip traces/dislocations etch-pits in Figure 8A–D. The slip traces or dislocation etch-pits continue in a specific direction before and after coming in contact with the intragranular pores.

4 | DISCUSSION

4.1 | Validation of deformation at room temperature

In STO, slip occurs on the $< 1\bar{1}0 > \{110\}$ slip systems at room temperature, which provides only two independent slip systems. However, the von Mises/Taylor criterion was proposed for bulk deformation with a focus on the interior grains. This shape change of interior grains is expressed in five independent strain parameters, including two normal strains (ε_{xx}, ε_{yy}) and three shear strains (γ_{xy}, γ_{yz}, γ_{xz}) under isovolumetric condition (i.e., $\varepsilon_{xx} + \varepsilon_{yy} + \varepsilon_{zz} = 0$).[17] Hence, five independent slip systems are required for general plastic deformation in all directions for interior grains. However, for surface grains, assuming $\varepsilon_{xx} = \varepsilon_{yy}$, for simplicity $\varepsilon_{zz} = 0$, and γ_{xy}, where ($\gamma_{yz} = \gamma_{xz} = 0$), resulting in only two active strain components (ε_{xx} and γ_{xy}). These two strain components are sufficient to accommodate the plastic deformation of surface grains, as suggested and observed by Chen et al.[44] on the surface grains of aluminum alloys during tensile deformation, hence satisfying the von Mises/Taylor criterion for limited deformation near/on the free surface.

Moreover, considering the cross section of the (001) orientation of single-crystal STO after 10× indentation in Figure 4D, the dislocation density decreases with increasing depth into the bulk, suggesting a gradient in the dislocation density with depth. This is due to the decaying shear stress field away from the contact region underneath the spherical indenter.[50] For Type X polycrystalline STO with an average grain size of 50 µm, high-density dislocations will most likely be accommodated within the (near) surface grains, limiting the influence of the interior grains and sub-surface GBs. Hence, the dislocation-based plastic deformation may be limited to the (near) surface grains where only two independent active slip systems are sufficient to accommodate a general shape change. However, consider that the cyclic Brinell indentation induced surface deformation can be extended to a much larger surface area by the cyclic Brinell scratching test (see Figure S4), that compensates the limited deformation depth but with large dislocation-rich areas for potential applications.

Besides the von Mises/Taylor criterion, there are other factors that can influence the plasticity of ceramics. It is preferable to avoid homogeneous dislocation nucleation because this requires very high stress levels. Hence, other sources of dislocations, such as heterogeneous nucleation and multiplication of dislocations from preexisting dislocations, grain boundary ledges, or triple junction pores, need to be examined for dislocation plasticity at lower stress levels, as will be discussed in the following sections.
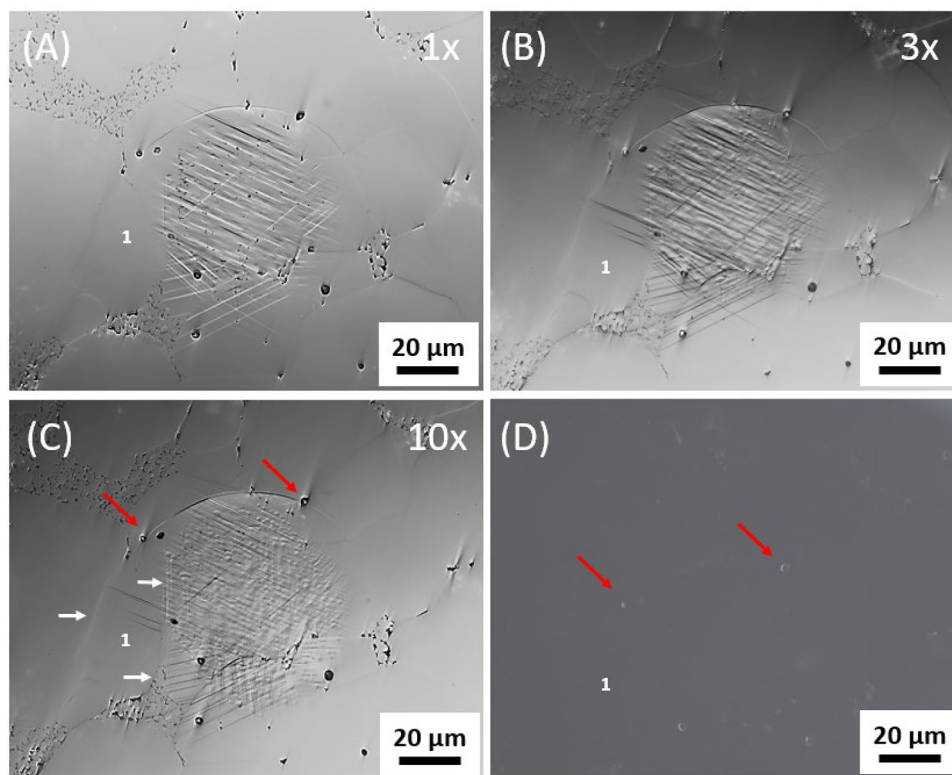
FIGURE 9 Optical image (A) after 1×, (B) 3×, and (C) 10× depicting the evolution of slip traces with increasing number of cycles. In position 1, the grain only depicted evidence of dislocation activity (slip traces) after 3× indentation. (D) Red arrows indicate the position of pores after 10× indentation, with no visible crack seen between them. White arrows indicate the grain boundaries for grain 1. (Dark-field image mode of in (D), captured after 10× indentation suggests that the impression connected by two pores indicated with red arrows is not a macroscopic crack. In the dark-field mode of optical microscopy, macroscopic cracks and surface pores would appear as bright spots.[58])

4.2 | Influence of grain boundaries and pores on dislocation mechanics

The initiation of slip from GB sources (GB ledges and triple junction pores) has been confirmed by different studies in metals[51] and ceramics.[28] Similar observations are presented in Section 3. Li[52] suggested that the GB ledges are non-regenerative, which means they do not produce Frank-Read sources. However, the sources of the dislocations in the current work must be regenerative as there are many more dislocations within the grains after 10× indentation compared to the 1× indentation (Figures 7A and 8E).

We propose a two-step deformation mechanism for the overall plasticity observed in Type X samples during cyclic Brinell indentation: The initial sources of the dislocations observed after the first cycle of indentation are most likely dominated by the GB boundary sources, and further indentation cycles are dominated by the multiplication mechanisms (such as Frank-Read sources and cross slip) within the individual grains. It is also important to note that not all GB sources are activated during the first cycle of indentation, and to this end, more insights are provided in Figure 9.

Contrary to the suggestion of Forty,[53] the intragranular pores present on the Type X sample did not impede the movement of dislocations. Instead, distinct slip traces cutting through the intragranular pores in Figures 7A,B, and 8 are observed, irrespective of the number of indentation cycles. It is commonly known that intergranular pores serve as stress concentration sites decreasing the interfacial strength between two adjacent grains, which makes them more susceptible to cracking (for instance, in brittle ceramics such as Al_2O_3[54]). In contrast, for polycrystalline STO plastically deformed using the Brinell indenter, the pores promote heterogeneous dislocation nucleation, accompanied by dislocation gliding at relatively lower applied stresses. Note that the yield strength of bulk single-crystal STO is ~120 MPa[55] suggesting easy dislocation glide in STO at room temperature. For context, the average stress P_m defined by the load (1.5 kgf) and the contact area with a contact radius a of (≈60 μm) is ~1.33 GPa for (001) single-crystal STO.[10] The resolved shear stress of 0.47 P_m acting on the {110}−45° planes will be ~625 MPa located underneath the surface about 0.5a,[10] even without considering the stress concentration effect induced by pores. This resolved shear stress is already much higher than the yield strength of single-crystal STO to move the generated

dislocations. Stokes and Li[56] suggested that intergranular pores in MgO act as dislocation sources, in line with our results. Moreover, the distribution of pores can play an important role in determining the plasticity and onset of cracking in the Type X sample. A cluster of pores would most likely induce cracks without appreciable plastic deformation. Moreover, the size of the pores relative to the average grain size could be a determinant factor for the competition between plasticity and cracking, as will be discussed in Section 4.3.

Additional tests were performed to capture the slip trace evolution after individual cycles on the same location. The most prominent results after 1×, 3×, and 10× are presented in Figure 9. After the first two cycles (1× in Figure 9A and 2× not presented here) of indentation, no evidence of dislocation activities (slip traces) was observed on the grain position 1. This observation serves as direct proof that not all grain boundary sources are activated after the first cycle of indentation.

The appearance of slip traces (in grain position 1) captured in Figure 9B after three cycles (3×) could be as a result of (i) the pile-up of mobile dislocations from the adjacent grain, exerting sufficient stress after three indentation cycles at the GB to activate slip in the adjacent grain (judging from the overall density of the slip traces after 3× indentation compared to 1× indentation) or (ii) the sources of dislocation within the grain 1 are activated by the transmission of dislocation from the adjacent grain. Compared to Figure 9C, there was no visually observable extension of the slip traces into other grains after 10× indentation cycles, but rather an increase in the slip trace density with the number of cycles similar to our observation in Sections 3.3 and 3.4, which further validates our earlier suggestion in this section, regarding the two-step deformation mechanism via cyclic Brinell indentation. Furthermore, a previous study of the interaction between dislocations and GBs in bi-crystal STO shows that the mobility of mechanically inserted dislocations is generally hindered by the grain boundary regardless of grain boundary structure.[57] This phenomenon is more pronounced for large angle GBs where dislocation pileup and subsequent cracking occur. However, future research is planned to address the impact of various GBs on the plastic deformation of polycrystalline strontium titanate.

4.3 | Effect of pore geometry on crack formation

The interfacial contact between two grains decreases when a pore is situated between them and may thus weaken the grain boundary. It is well known that pores can act as stress concentrators to induce cracks in most ceramics. Based
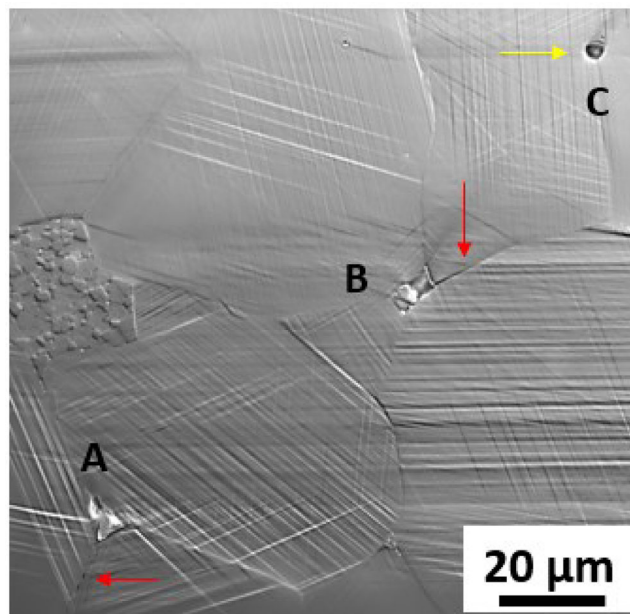

FIGURE 10 Optical microscope image after 1× indentation demonstrating the propagation of crack (indicated using red arrows) from triple junction pores with diameter (A = 9 μm, B = 7 μm), and pore size of 2 μm indicted with yellow arrow (position C) only involved in dislocation activity.

on what we observed before, the pores in *ductile* ceramics such as $SrTiO_3$ can also serve as nucleation sites for dislocations. Langdon et al.[59] observed an overall loss in ductility with increasing pore size to grain size ratio on the plasticity of MgO over a large temperature range (up to 1400°C). A large pore size to grain size ratio means a high stress concentration that potentially leads to cracking.

A distinct feature in Figure 10 is the shape of the pores. Both pores on positions A and B have sharp edges, which serve as more effective stress concentrators irrespective of the pore size. The nucleation of cracks from sharp-edged pores was also observed in Figure 7B (pore on the grain boundary between grains 1 and 8). A negating trend is observed for pores with near circular geometry, contributing to dislocation activity while avoiding cracking as seen in Figures 8F and 10 (position C). A theoretical study by Fischer et al.[60] suggests the competition between dislocation nucleation and crack propagation depends on the geometry of the flaws (e.g., cracks or pores). A well-defined pore size, geometry, and spatial distribution[61] can be envisaged to impact the plastic deformation of *ductile* ceramics even at room temperature.

Lastly, we also note the possible influence of defect chemistry, which could impact the dislocation-based plasticity of the three polycrystalline STO samples. Conventional sintering (Type X) was performed in an oxygen-rich atmosphere with a final annealing step in a reducing atmosphere, which in turn increases the oxygen vacancy

concentration.[40] On the other hand, flash sintering (Type Y) generally leads to samples with gradient (both point defects, particularly oxygen vacancies, and grain size).[41] The large average-grain-size region (Type Y1) is at the negative electrode with an enriched oxygen vacancy concentration as compared to the small average-grain-size region (Type Y2) with a depleted oxygen vacancy concentration.[41] In a separate study via nanoindentation,[62] the influence of oxygen vacancy concentration has been reported to favor dislocation nucleation while impeding the motion of dislocations on single crystal STO. However, the impact of the defect chemistry on the plastic deformation of polycrystalline STO is out of the scope of this work and is planned for future study.

5 | CONCLUSION

Room-temperature dislocation-mediated plastic deformation of polycrystalline strontium titanate was studied using the cyclic Brinell indentation method. Deformation tests on single-crystal (001), (011), and (111) samples were additionally performed, serving as benchmarking on the crystallographic influence. Dislocation-mediated plastic deformation (with plastic zone size ~120 µm in diameter with a load of 1.5 kgf and an indenter diameter of 2.5 mm) on the surface of coarse-grained polycrystalline $SrTiO_3$ (with an average grain size of 50 µm) was successfully generated via room-temperature cyclic indentation without macroscopic surface cracking. This is attributed to the free surface relaxation that avoids dislocation pile-up and surface crack formation. An overall increase in dislocation density was observed in both polycrystalline and single-crystal samples after deformation with increased cycle number. For all polycrystalline samples tested, the plastic zone size and deformation impression depth decreased with the grain size, indicating grain boundary strengthening. Counter-intuitive to most brittle ceramics at room temperature, the grain boundary ledges and triple junction pores in *ductile* ceramics appear to act as sources for dislocation generation and multiplication, facilitating plastic deformation for the deformable ceramics. We propose a two-step mechanism for the plastic deformation by cyclic indentation, where the first-cycle indentation is dominated by the activation of dislocation sources at GBs as well as grain interiors, and further indentation during cyclic loading is dominated by dislocation multiplication. We expect the findings on polycrystalline $SrTiO_3$ to be transferrable to other ceramics that exhibit room-temperature plasticity. The preliminary examination of the grain-size dependent study in this work may pave the road for future studies on the geometrical contribution and grain size effect on dislocation-GB interaction.

ORCID

Neamul Khansur https://orcid.org/0000-0001-8769-3329
Xufei Fang https://orcid.org/0000-0002-3887-0111

REFERENCES

1. Fang X, Nakamura A, Rödel J. Deform to perform: dislocation-tuned properties of ceramics. Am Ceram Soc Bull. 2023;102:24–29.
2. Fang X. Mechanical tailoring of dislocations in ceramics at room temperature: a perspective. J Am Ceram Soc. 2023;107(3):1425–47.
3. Ikuhara Y. Nanowire design by dislocation technology. Prog Mater Sci. 2009;54(6):770–91.
4. Nakamura A, Lagerlöf KPD, Matsunaga K, Tohma J, Yamamoto T, Ikuhara Y. Control of dislocation configuration in sapphire. Acta Mater. 2005;53(2):455–62.
5. Mitchell T, Lagerlöf KP. Dislocations in ceramics. Mater Sci Technol. 1985;1:944–49.
6. Argon AS, Orowan E. Plastic deformation in MgO single crystals. Philos Mag J Theor Exp Appl Phys. 1964;9(102):1003–21.
7. Phillips Jr. WL. Deformation and fracture processes in calcium fluoride single crystals. J Am Ceram Soc. 1961;44(10):499–506.
8. Mark AF, Castillo-Rodriguez M, Sigle W. Unexpected plasticity of potassium niobate during compression between room temperature and 900°C. J Eur Ceram Soc. 2016;36(11):2781–93.
9. Gilman JJ, Johnston WG. Dislocations in lithium fluoride crystals. In: Seitz F, Turnbull D, editors. Solid state physics. Cambridge: Academic Press; 1962. p. 147–222.
10. Okafor C, Ding K, Zhou X, Durst K, Rödel J, Fang X. Mechanical tailoring of dislocation densities in $SrTiO_3$ at room temperature. J Am Ceram Soc. 2022;105(4):2399–402.
11. Fang X, Preuß O, Breckner P, Zhang J, Lu W. Engineering dislocation-rich plastic zones in ceramics via room-temperature scratching. J Am Ceram Soc. 2023;106(8):4540–45.

12. Preuß O, Bruder E, Lu W, Zhuo F, Minnert C, Zhang J, et al. Dislocation toughening in single-crystal $KNbO_3$. J Am Ceram Soc. 2023;106(7):4371–81.

13. Oshima Y, Nakamura A, Matsunaga K. Extraordinary plasticity of an inorganic semiconductor in darkness. Science. 2018;360(6390):772–74.

14. Anderson PM, Hirth JP, Lothe J. Theory of dislocations. Cambridge: Cambridge University Press; 2017.

15. Mises RV. Mechanik der plastischen Formänderung von Kristallen. ZAMM—J Appl Math Mech/Z Angew Math Mech. 1928;8(3):161–85.

16. Taylor G I. Plastic strain in metals. J Inst Metals. 1938;62:307–24.

17. Groves GW, Kelly A. Independent slip systems in crystals. Philos Mag. 1963;8(89):877–87.

18. Kacher J, Eftink BP, Cui B, Robertson IM. Dislocation interactions with grain boundaries. Curr Opin Solid State Mater Sci. 2014;18:227–43.

19. Shen Z, Wagoner RH, Clark WAT. Dislocation and grain boundary interactions in metals. Acta Metall. 1988;36(12):3231–42.

20. Bayerschen E, McBride AT, Reddy BD, Böhlke T. Review on slip transmission criteria in experiments and crystal plasticity models. J Mater Sci. 2016;51(5):2243–58.

21. Stroh AN. The formation of cracks as a result of plastic flow. Proc R Soc London, Ser A Math Phys Sci. 1954;223:404–14.

22. Zener C. The micro-mechanism of fracture. In: Fracturing of metals. Berlin: Springer; 1948. Vol. 3. p. 551–90.

23. Porz L, Klomp AJ, Fang X, Li N, Yildirim C, Detlefs C, et al. Dislocation-toughened ceramics. Mater Horiz. 2021;8(5):1528–37.

24. Porz L, Scherer M, Höfling M, Nakamura A, Rheinheimer W, Rödel J. Dislocation-based high-temperature plasticity of polycrystalline perovskite $SrTiO_3$. J Mater Sci. 2023;58(6):2430–38.

25. Johanning M, Porz L, Dong J, Nakamura A, Li JF, Rödel J, et al. Influence of dislocations on thermal conductivity of strontium titanate. Appl Phys Lett. 2020;117(2):021902.

26. Fang X, Ding K, Janocha S, Minnert C, Rheinheimer W, Frömling T. Nanoscale to microscale reversal in room-temperature plasticity in $SrTiO_3$ by tuning defect concentration. Scr Mater. 2020;188:228–32.

27. Fang X, Bishara H, Ding K, Tsybenko H, Porz L, Höfling M, et al. Nanoindentation pop-in in oxides at room temperature: dislocation activation or crack formation? J Am Ceram Soc. 2021;104(9):4728–41.

28. Sinha MN, Lloyd DJ, Tangri, K. Microyield and fracture in polycrystalline MgO. J Mater Sci. 1973;8:116–22.

29. Scott WD, Pask JA. Deformation and fracture of polycrystalline lithium fluoride. J Am Ceram Soc. 1963;46(6):284–93.

30. Nadgornyi EM, Strunk HP. Dislocation structure of plastically deformed NaCl polycrystals. Phys Status Solidi A. 1987;104(1):193–202.

31. Westwood ARC. On the fracture behaviour of magnesium oxide bi-crystals. Philos Mag. 1961;6(62):195–200.

32. Moriyoshi Y, Kingery W, Vander Sande J. Fracture in magnesium oxide bicrystals. J Mater Sci. 1977;12:1062–64.

33. Taeri S, Brunner D, Sigle W, Rühle M. Deformation behaviour of strontium titanate between room temperature and 1800 K under ambient pressure. Int J Mater Res. 2004;95(6):433–46.

34. Hull D, Bacon DJ. Dislocation arrays and crystal boundaries. In: Hull D, Bacon DJ, editors. Introduction to dislocations. 5th ed. Oxford: Butterworth-Heinemann; 2011. p. 171–204.

35. Pelleg J. Mechanical properties of ceramics. Berlin: Springer Science & Business; 2014.

36. Snowden WE, Pask JA. High-temperature deformation of polycrystalline magnesium oxide. Philos Mag. 1974;29(3):441–55.

37. Day RB, Stokes RJ. Mechanical behavior of polycrystalline magnesium oxide at high temperatures. J Am Ceram Soc. 1966;49(7):345–55.

38. Pelleg J, Pelleg J. Creep in ceramics. Berlin: Springer; 2017.

39. Borowski M. Perovskites: structure, properties, and uses. New York: Nova Science Publishers; 2010.

40. Rheinheimer W, Bäurer M, Hoffmann MJ. A reversible wetting transition in strontium titanate and its influence on grain growth and the grain boundary mobility. Acta Mater. 2015;101:80–89.

41. Rheinheimer W, Phuah XL, Wang H, Lemke F, Hoffmann MJ, Wang H. The role of point defects and defect gradients in flash sintering of perovskite oxides. Acta Mater. 2019;165:398–408.

42. Rheinheimer W, Phuah XL, Porz L, Scherer M, Cho J, Wang H. The impact of flash sintering on densification and plasticity of strontium titanate: high heating rates, dislocation nucleation and plastic flow. J Eur Ceram Soc. 2023;43(8):3524–37.

43. Akedo J. Aerosol deposition of ceramic thick films at room temperature: densification mechanism of ceramic layers. J Am Ceram Soc. 2006;89(6):1834–39.

44. Chen P, Mao SC, Liu Y, Wang F, Zhang YF, Zhang Z, et al. In-situ EBSD study of the active slip systems and lattice rotation behavior of surface grains in aluminum alloy during tensile deformation. Mater Sci Eng: A. 2013;580:114–24.

45. Schmid E, Boas W. Geometrie der Kristall-Deformationsmechanismen, Kristallplastizität: Mit Besonderer Berücksichtigung der Metalle. Berlin, Heidelberg: Springer; 1935. p. 58–80.

46. Hall EO. The deformation and ageing of mild steel: III Discussion of results. Pro Phys Soc Sec B. 1951;64(9):747.

47. Petch N. The cleavage strength of polycrystals. J Iron Steel Inst. 1953;174:25–28.

48. Salem M, Ding K, Rödel J, Fang X. Thermally enhanced dislocation density improves both hardness and fracture toughness in single-crystal $SrTiO_3$. J Am Ceram Soc. 2023;106:1344–55.

49. Javaid F, Stukowski A, Durst K. 3D dislocation structure evolution in strontium titanate: spherical indentation experiments and md simulations. J Am Ceram Soc. 2017;100:12.

50. Swain MV, Lawn BR. A study of dislocation arrays at spherical indentations in LiF as a function of indentation stress and strain. Phys Status Solidi. 1969;35(2):909–23.

51. Worthington PJ, Smith E. The formation of slip bands in polycrystalline 3% silicon iron in the pre-yield microstrain region. Acta Metall. 1964;12(11):1277–81.

52. Li JC. Petch relation and grain boundary sources. Trans Metall Soc AIME. 1963;227(1):239.

53. Forty AJ. Interaction of cavities and dislocations in crystals. Discuss Faraday Soc. 1964;38:56–60.

54. Flinn BD, Bordia RK, Zimmermann A, Rödel J. Evolution of defect size and strength of porous alumina during sintering. J Eur Ceram Soc. 2000;20(14):2561–68.

55. Gumbsch P, Taeri-Baghbadrani S, Brunner D, Sigle W, Rühle M. Plasticity and an inverse brittle-to-ductile transition in strontium titanate. Phys Rev Lett. 2001;87(8):085505.

56. Stokes RJ, Li CH. Dislocations and the tensile strength of magnesium oxide. J Am Ceram Soc. 1963;46(9):423–34.

57. Kondo S, Mitsuma T, Shibata N, Ikuhara Y. Direct observation of individual dislocation interaction processes with grain boundaries. Sci Adv. 2016;2(11):e1501926.

58. Vander Voort GF, Committee AH. Visual examination and light microscopy. In: Fractography. Detroit: ASM International; 1987. p. 91–165.

59. Langdon TSG, Pask JA. Effect of microstructure on deformation of polycrystalline MgO. J Am Ceram Soc. 1971;54(5):240–46.

60. Fischer LL, Beltz GE. The effect of crack blunting on the competition between dislocation nucleation and cleavage. J Mech Phys Solids. 2001;49(3):635–54.

61. Zimmermann A, Hoffman M, Flinn BD, Bordia RK, Chuang TJ, Fuller Jr. ER, et al. Fracture of alumina with controlled pores. J Am Ceram Soc. 1998;81(9):2449–57.

62. Stich S, Ding K, Muhammad QK, Porz L, Minnert C, Rheinheimer W, et al. Room-temperature dislocation plasticity in SrTiO$_3$ tuned by defect chemistry. J Am Ceram Soc. 2022;105(2):1318–29.

SUPPORTING INFORMATION

Additional supporting information can be found online in the Supporting Information section at the end of this article.